Differential Absorption Lidar to Measure Sub-hourly Variation of Tropospheric Ozone Profiles

Shi Kuang[1], John F. Burris[2], Michael J. Newchurch[1*], Steve Johnson[3] , and Stephanie Long[4]

[1] *Atmospheric Science Department, University of Alabama in Huntsville, 320 Sparkman Dr., Huntsville, Alabama 35805, USA*

[2] *NASA-Goddard Space Flight Center, Code 694, Greenbelt, Maryland 20771, USA*

[3] *NASA-Marshall Space Flight Center, Office Code VP61, Huntsville, Alabama 35812, USA*

[4] *Department of Physics, University of Alabama in Huntsville, Huntsville, Alabama 35805, USA*

*Corresponding author: mike@nsstc.uah.edu

7/30/09

Submit to *IEEE Transactions on Geoscience and Remote Sensing*

This work was supported by NASA's Science Mission Directorate and NOAA's National Enviromental Satellite, Data, and Information Service (NESDIS).

Index Terms – DIAL, Lidar, Ozone, Remote sensing, Troposphere.

ABSTRACT: A tropospheric ozone Differential Absorption Lidar (DIAL) system, developed jointly by the University of Alabama at Huntsville and NASA, is making regular observations of ozone vertical distributions between 1 and 8 km with two receivers under both daytime and nighttime conditions using lasers at 285 and 291 nm. This paper describes the lidar system and analysis technique with some measurement examples. An iterative aerosol correction procedure reduces the retrieval error arising from differential aerosol backscatter in the lower troposphere. Lidar observations with coincident ozonesonde flights demonstrate that the retrieval accuracy ranges from better than 10% below 4 km to better than 20% below 8 km with 750-m vertical resolution and 10-min temporal integration.

1. Introduction

Ozone is a key trace-gas species within the troposphere. Although ozone is a precursor of the hydroxyl radical, which reacts with most trace species in the atmosphere, ozone is also a strong greenhouse gas influencing the climate by its radiative forcing and is a direct pollutant [1]. In situ photochemistry and dynamic processes largely govern the distribution of tropospheric ozone [2]. Measuring ozone variability at high spatial and temporal resolution increases our understanding of tropospheric chemistry [3, 4], planetary boundary layer (PBL)–free-tropospheric exchange [5, 6] stratosphere-troposphere exchange (STE) [7-9] and the impact of lightning-generated NOx on tropospheric ozone [10-13].

Several techniques currently exist for making range-resolved measurements of tropospheric ozone. The most common technique is the balloon-borne electrochemical concentration cell (ECC), which has monitored ozone since the 1960's. The ozonesonde profiles ozone with a 100-m vertical resolution from the surface to 35-km altitude with the accuracy of

5-10% [14, 15]. Ozonesondes are attractive because of their low upfront cost and well-characterized behavior. However, they are not suitable for making continuous measurements because of logistical considerations. Interesting atmospheric phenomena that vary over periods less than one day are particularly difficult to monitor using balloon ozonesondes. Satellite observations can derive total column ozone [16], stratospheric ozone [17-21], and extend measurements to altitudes that are inaccessible to ozonesondes. More recently, high-quality satellite observations of tropospheric ozone are becoming available [17, 22-30]. Although the satellite measurements can produce global maps of ozone, their current measurement uncertainties along with their coarse spatial and temporal resolution limit their ability to observe short-term variations in ozone. Lidars can supplement these techniques when a requirement exists for ozone retrievals with higher temporal (from 1 min to several hours) and vertical resolution (from tens of meters to 2 km). For example, lidars of the Network for the Detection of Atmospheric Composition Change (NDACC) [31, 32] are providing long-term observations of ozone as well as aerosol, temperature, and water vapor. Although the upfront costs are considerably higher than for a balloon ozonesonde operation, lidars can acquire profiles continuously under both daytime and nighttime conditions. The spatial and temporal resolution of a lidar is more than sufficient to characterize short-term ozone variations for the photochemical studies of vertical processes.

Differential Absorption Lidar (DIAL) has been successfully used to measure ozone within the PBL [33, 34], the free-troposphere [35-40], and the stratosphere [41-44] for several decades. DIAL is evolving from ground-based and airborne systems to systems suitable for long-term deployment in space [45]. The technique derives ozone concentrations by analyzing how rapidly the backscattered signals at two separate but closely spaced wavelengths, one strongly absorbed by ozone and the other less strongly absorbed, diminish with altitude. This measurement does not require the absolute signal intensities but only how the relative change of the two signals with respect to altitude. The wavelengths optimize the differential absorption of ozone and minimize differential extinction due to aerosols, SO_2, and other species. Using electronically-gated detection permits range-resolved measurements to a resolution as small as several meters over acquisition times of several minutes. The location of the ozone DIAL discussed in this paper in the southeastern United States provides a unique observational site within an interesting scientific area [46] to study trace gas transport at the mid-latitudes for both the polluted PBL and the free troposphere.

2. System Description

Housed in the Regional Atmospheric Profiling Center for Discovery (RAPCD), the tropospheric ozone DIAL system is located at 34.7250°N, 86.6450°W on the campus of the University of Alabama in Huntsville (UAHuntsville) within the Huntsville city limits at an elevation of 206 m ASL. It is designed for measurements within the PBL and the free-troposphere during both daytime and nighttime. Because of UAHuntsville's location and occasional high temperature and humidity conditions, heavy aerosol pollution is sometimes present. Compared with the clean free-troposphere, these aerosols require a larger dynamic range for the detection system because of their larger optical depth. Moreover, the rapid change of aerosol concentrations (e.g., due to convective activity) increases the measurement uncertainty for DIAL within the PBL and lower troposphere. Judicious system–design choices and an effective aerosol-correction scheme allow this system to produce high-quality ozone profiles under a variety of conditions.

2.1 Wavelength selection

The selection of the 285- and 291-nm wavelengths results from the balance of the following three considerations: 1) optimizing the altitude range to make retrievals; 2) reducing the impact of the solar background during daytime operation; 3) reducing the impact of aerosol interference upon the ozone retrieval. The DIAL wavelength selection is flexible and optimized for the local ozone distribution, the absorption arising from non-ozone species, the measurement range and the specific system configuration including the output power, telescope mirror size, and the photomultiplier's (PMT's) dynamic range. Numerous publications (e.g., Megie et al. [47]) discussed the optimum wavelengths for tropospheric systems. Although shorter wavelengths can provide higher measurement sensitivity arising from the larger ozone differential cross-section, they limit the maximum measurable range due to stronger attenuation of ozone absorption and Rayleigh (molecular) extinction, and thus, require more signal acquisition time. In addition, the shorter wavelengths require more dynamic range of the detection system and might require more altitude channels. With the current transmitter power, the on-line wavelength of 285 nm allows us to measure ozone up to 9 km under a clear sky and 7 km under aerosol loading with a 10-min temporal resolution. Because of the increasing solar background during daytime operations, we choose 291 nm as the off-line wavelength. Longer wavelengths will cause a significant increase in the solar background and reduce the signal-to-background ratio. To measure both wavelength channels using the same PMT and simplify the system design, we used a band-pass filter with a central wavelength of 286.4 nm and a full width at half maximum (FWHM) of 11 nm whose transmittance is $\leq 10^{-8}$ at wavelengths longer than 300 nm. For a band-pass filter, the integrated sky background over the filter bandwidth and the dark counts actually determine the background for both off-line and on-line wavelengths. For our lidar configuration, the 285 and 291-nm wavelength region can provide sufficient signal-to-background ratios at 8 km under most sky conditions. The retrieval errors due to aerosol interference are a concern in the PBL and lower troposphere. These errors are not a simple function of the wavelength separations because reducing the separation to reduce the aerosol differential backscattering will also decrease the differential ozone cross-section. These errors are sensitive to the local aerosol composition, size distribution, and vertical profile. Although the aerosol interference can be lower when our on-line wavelength extends to the steepest part of the ozone absorption cross section, this will significantly sacrifice the maximum measurable range. Therefore, the 285-291 nm pair is the optimal choice to balance the maximum measurable altitude, the impact of aerosol differential backscattering, and the impact of solar background.

2.2 Hardware components

Table 1 lists the characteristics of the RAPCD ozone DIAL system. The transmitter consists of two identical dye lasers pumped by two separate, frequency-doubled Nd:YAG lasers (Figure 1). A pulse generator triggers each laser pulse with a 25-ms separation between the alternate pulses. The dye lasers are software-controlled to select the user-defined wavelength. The knife-edge method [48] determines that the divergences of both UV laser beams are less than 1 mrad. A 0.75-m triple grating monochromator (Acton Research Corporation) indicates that the actual wavelengths of the outgoing UV lasers are 285 and 291 nm within an uncertainty of 0.1 nm.

The receiving system currently operates with two separate telescopes as shown in Figure 2. The high-altitude receiver uses a 40-cm Newtonian telescope, and the low-altitude channel employs a 10-cm Cassegrain telescope. The large telescope system routinely makes measurements from 3 to 8 km and on occasion has reached 12 km. Employing a 1.5-mrad field-of-view (FOV), the large telescope achieves full overlap between the laser and receiver at about 3 km. Larger FOVs lower the altitude at which full overlap occur but significantly increase solar background. The small telescope system currently retrieves ozone between 1 and about 5 km with a typical

FOV of 4.3 mrad. The future plan is to extend the retrievals down to about 200 m with an additional altitude channel in the small telescope. The band-pass filters used to restrict the solar background for both receivers have a transmittance of 35% at 285 nm and 20% at 291 nm.

The detection system of the RAPCD ozone DIAL uses both photon counting and analog detection to facilitate operations over both altitude channels. This detection combination provides the linearity of the analog signal in the strong-signal region and high sensitivity of the photon-counting signal in the weak-signal region. A EMI 9813 QA PMT, which has been used extensively for many years on a number of Goddard Space Flight Center lidar system [49, 50] is used in the high-altitude channel while a small Hamamatsu 7400 PMT is used in the low-altitude channel. A photodiode detects the outgoing laser pulses, which trigger both the PMT gating circuits and the LICEL Transient Recorder (TR40-80, LICEL Company, Germany). The LICEL-TR offers the advantage of increased dynamic range by providing simultaneous measurements using both analog detection and photon counting. The LICEL-TR's highest temporal resolution is 25 ns corresponding to a fundamental range resolution of 3.75 m. It is necessary to gate the high-altitude channel off for the first 10-15 μs and the low-altitude channel for the first 1 μs to maintain the PMT's linearity and minimize the impact of signal-induced bias on the background count rate.

3. Data processing

3.1 Raw data processing

Several operations, designed to improve the measurement precision, occur before the ozone retrieval. First, average the signal returns over 10 min and 150 m. The temporal resolution of the retrieval can be varied depending on the signal-to-noise ratio (SNR). Second, apply a dead-time correction to the photoncounting (PC) signals. For PC at high counting rates, a second pulse arriving at the discriminator before it has recovered from the previous pulse will not be counted – a period known as dead time [51]. Experiments with a function-generator-driven LED determine this time to be 10 ns for the high-altitude channel and 4 ns for the low-altitude channel. Our results show that the system dead time obeys a nonparalyzable model following a simple relationship, Eq. (1) [52], between the true count rate, C_T, and measured count rates, C_M, allowing the impact of dead time, T_d, on the data to be removed.

$$C_T = \frac{C_M}{1 - C_M T_d}. \qquad (1)$$

Third, remove background counts due to PMT dark counts and the sky background. Both of these counts are constant over all ranges and can be derived using data bins for which there are no laser signal returns. Fourth, glue the parallel analog and PC signals together [53]. The analog signal associated with the use of LICEL has a small time delay relative to the PC signal [54]. We found this offset to be about 250 ns for our system by carefully comparing returns derived with clouds on both the analog and PC channels. The glued signal must first account for this offset. The glued region requires that the ratio of PC to analog signal is constant. Ratios that are not constant suggest either an incorrect background subtraction or wrong dead-time correction. The gluing threshold of the PC signal is typically 20 MHz for the Hamamatsu PMT employed in our low-altitude channel and 20-30 MHz for the EMI PMT used on the high-altitude channel. Because DIAL retrievals depend on the quality of both 285 and 291 signal, we glue the PC and analog signal approximately at the same altitude for both lasers to minimize the retrieval error due to gluing. Examples of the ratio of PC-to-analog signal and their gluing region for 285-nm signal appear in the Figure 3. The gluing threshold is 20 MHz for both altitude channels. The fifth step involves smoothing the counts to reduce random noise. Our configuration currently employs a 5-point ($5 \times 150 = 750m$) running average applied to returns from all altitudes; smoothing reduces the effective vertical resolution to 750 m.

After initial processing, an exponential-fit correction removes signal-induced bias (SIB) from the signal returns. This bias, caused by intense light returns from near range, (also called signal-induced noise, SIN) appears as a slowly decaying noise source superimposed on the normal returns. The causes of the SIB are related to the regenerative effects such as dynode glow, after-pulsing, glass-charging effect, shielding effect, and helium penetration [55]. SIB varies widely with different PMTs. For our case, the SIB of the EMI 9813 is larger than for the Hamamatsu 7400. SIB can persist for several hundred microseconds and can exert a strong influence on data at the lidar's upper range where both signal and noise counts become comparable. With uncorrected SIB, the raw signal falls off more slowly at higher altitudes resulting in lower retrieved ozone values. SIB usually has more influence on the shorter wavelength channel, which falls off more rapidly with altitude. Unless a mechanical shutter physically blocks the optical path to the PMT to eliminate SIB, a model must characterize its behavior. Cairo et al. [56] and Zhao [57] have successfully used a double exponential function for this purpose. However, this correction increases measurement uncertainties because both the scaling and exponential lifetimes are difficult to determine without additional independent measurements. A more practical technique is to employ a single exponential fit to the residual background [39, 40, 58]. For the high-altitude channel, the function's coefficients are automatically determined using a single exponential least-squares fit to data acquired approximately from 100 to 160 μs after data acquisition starts where the SIB becomes dominant. The start and length of the exponential fit varies with different channels (either wavelength channels or altitude channels), atmospheric structures, and lidar configurations because these parameters affect the intensity of the detected signal. For our low-altitude channel, the SIB is weaker than the high-altitude channel because of the different PMT and weaker signal. However, it is difficult to automatically determine the fitting function for the low-altitude channel signal using the least-squares fitting method especially for the 285 signal because the far-range signal after background correction is not completely characterized by an exponential function (Figure 3 (b)). It is useful to optimize the exponential fitting function for the low-altitude channel using previous retrieval data and comparing the data with coincident ozonesonde profiles. The slope of the logarithm of the SIB fitting function remains for a particular configuration (i.e., outgoing power) and could slightly change for different configurations. Those retrievals corrected using the empirically-derived exponential function agree with ozonesonde profiles up to 5 km within 5% bias. Figure 3 shows the typical effect of the SIB correction and the comparison of the fully corrected signal and model for 285-nm signal. The model simulation employs the coincident ozonesonde measurement assuming no aerosol.

3.2 DIAL retrieval

The differential technique reduces the ozone retrieval uncertainty resulting from interfering aerosols and non-ozone gases. Excellent discussions concerning the DIAL technique occur in the publications by Measures [59], Kovalev and Eichinger [60], and Browell [36]. The average ozone number density, $n_{(r+\Delta r/2)}$, between range r and $r+\Delta r$ can be expressed as the summation of the signal term, $n^{s}_{(r+\Delta r/2)}$, the differential backscattering term, $\Delta n^{b}_{(r+\Delta r/2)}$, and the differential extinction term, $\Delta n^{e}_{(r+\Delta r/2)}$, as following equation:

$$n_{(r+\Delta r/2)} = n^{s}_{(r+\Delta r/2)} + \Delta n^{b}_{(r+\Delta r/2)} + \Delta n^{e}_{(r+\Delta r/2)}. \qquad (2)$$

One can write the discrete forms of the three terms at right side as follows:

$$n^{s}_{(r+\Delta r/2)} = \frac{1}{2\Delta r \Delta\sigma_{O3}} \ln\left(\frac{P_{on(r)} P_{off(r+\Delta r)}}{P_{off(r)} P_{on(r+\Delta r)}}\right), \tag{3}$$

$$\Delta n^{b}_{(r+\Delta r/2)} = -\frac{1}{2\Delta r \Delta\sigma_{O3}} \ln\left(\frac{\beta_{on(r)} \beta_{off(r+\Delta r)}}{\beta_{off(r)} \beta_{on(r+\Delta r)}}\right), \tag{4}$$

$$\Delta n^{e}_{(r+\Delta r/2)} = -\frac{1}{\Delta\sigma_{O3}} (\alpha_{on(r+\Delta r/2)} - \alpha_{off(r+\Delta r/2)}), \tag{5}$$

where the subscript ‘on’ and ‘off’ represent the on-line (285 nm) and off-line (291 nm) wavelengths, respectively; P is the detected photon counts; β is the total backscatter coefficient; α is the total extinction coefficient excluding ozone, and $\Delta\sigma_{O3}$ is the differential ozone absorption cross-section. P, β, and α are dependent on r and wavelength. Strictly speaking, $\Delta\sigma_{O3}$ is a r dependent, as well, because it is a function of temperature, which varies with r. By ignoring the differential scattering and extinction from non-ozone species, the DIAL equation reduces to only n^{s}. Δn^{b} arises from aerosol differential backscattering. Δn^{e} consists of differential Rayleigh extinction, aerosol extinction, and non-ozone gaseous absorption including O_2, SO_2 and NO_2. Measurements from a meteorological sounding can usually correct Rayleigh effects. We correct the aerosol effects when they are significant enough, especially in PBL. The aerosol correction discussion appears in Section 3.4.

3.3 Joining retrievals from two adjacent altitude channels

Final retrievals result from joining the data from two altitude channels with a weighted average. We choose to join the final ozone retrievals instead of the raw signals because the SNRs of the two altitude channels at the joining altitude are significantly different. If the retrievals derived from two different channels are statistically independent, the best estimate of these measurements is the 2-channel weighted average: [61]

$$n_{best} = \sum_{i=1}^{2} w_i n_i / \sum_{i=1}^{2} w_i \,, \tag{6}$$

where n_i is the ozone retrievals of channel i and the weights w_i are the inverse squares of the corresponding statistical uncertainties (ε_{1i}, which will be discussed in Section 5),

$$w_i = 1/\varepsilon_{1i}{}^2 \,. \tag{7}$$

The uncertainty of n_{best} is

$$\varepsilon_{1best} = \left(\sum_{i=1}^{2} w_i \right)^{-1/2} . \tag{8}$$

Typically, the low-altitude and high-altitude channels join between 3.3 and 4.4 km. Figure 4 shows an example of a joined ozone profile as well as the combined 1-sigma statistical uncertainties.

3.4 Aerosol correction

In a polluted area, aerosols can be a dominant error source in the lower troposphere. Based on Eq. (4) and (5), The vertical gradient of aerosol backscattering determines Δn^b and the magnitude of the differential aerosol extinction coefficient determines Δn^e . The largest aerosol correction usually occurs in an inhomogeneous aerosol layer (i. e., the top of the PBL). One can solve for the ozone and aerosol profiles simultaneously with only two wavelengths by assuming appropriate Ångström exponents and constant lidar ratios [62, 63]. If a third wavelength is available, and is close to the DIAL wavelength pair, one can use the dual-DIAL technique [64, 65] to reduce the error due to aerosol. When the third wavelength is far from the DIAL wavelength pair, one can use the method suggested by Browell [36] to correct the aerosol interference. Without the third wavelength, we employ an iterative procedure to retrieve ozone and correct aerosol effects. To illustrate this method, start from the equation to solve for the ozone using only the 291-nm signal [59]:

$$n_{(r+\Delta r/2)} = \frac{1}{2\sigma_{O3}\Delta r} \times \{\ln(\frac{P_{(r)}}{P_{(r+\Delta r)}}) - \ln[\frac{(\beta^M_{(r)} + \beta^A_{(r)})/r^2}{(\beta^M_{(r+\Delta r)} + \beta^A_{(r+\Delta r)})/(r+\Delta r)^2}] - 2(\alpha^M_{(r+\Delta r/2)} + \alpha^A_{(r+\Delta r/2)})\Delta r\}\,, \quad (9)$$

where σ_{O3} is the ozone absorption cross-section; $\beta^M_{(r)}$ and $\beta^A_{(r)}$ are molecular and aerosol backscatter coefficients at range r, respectively; $\alpha^M_{(r+\Delta r/2)}$ and $\alpha^A_{(r+\Delta r/2)}$ represent the average molecular and aerosol extinction coefficients respectively between range r and $r + \mathrm{D}r$. The subscript 291 is omitted for brevity, because all backscatter and extinction parameters correspond to 291 nm. Assuming the lidar ratio (aerosol extinction-to-backscatter ratio), S, is known for the 291-nm signal:

$$S = \alpha^A / \beta^A, \quad (10)$$

Solving for $\beta^A_{(r)}$, Eq. (9) becomes:

$$\beta^A{}_{(r)} = \exp\{\ln(\frac{P_{(r)}}{P_{(r+\Delta r)}}) - 2n_{(r+\Delta r/2)}\sigma_{O3}\Delta r - 2(\alpha^M_{(r+\Delta r/2)} + \alpha^A_{(r+\Delta r/2)})\Delta r\}\frac{r^2(\beta^M_{(r+\Delta r)} + \beta^A_{(r+\Delta r)})}{(r+\Delta r)^2} - \beta^M_{(r)}, \quad (11)$$

For *S* constant with range, a priori $\beta^A_{(ref)}$ at reference range, and downward numerical calculation, only one unknown variable, $\alpha^A_{(r+\Delta r/2)}$, remains in Eq. (11). If we further assume:

$$\alpha^A_{(r+\Delta r/2)} \approx \alpha^A_{(r+\Delta r)} = S\beta^A_{(r+\Delta r)}, \quad (12)$$

and $\beta^A_{(ref)}$ is zero at the reference range. The $\beta^A_{(r)}$ can be solved by Eq (11) starting from the reference range and calculating downward. Then, the first estimate for $\beta^A_{(r)}$ profile is substituted back into Eq. (11) to get the second estimate. However, we can use a more accurate form for $\alpha^A_{(r+\Delta r/2)}$ as:

$$\alpha^A_{(r+\Delta r/2)} = S(\beta^A_{(r+\Delta r)} + \beta^{A\,'}_{(r)})/2, \quad (13)$$

where $\beta^{A'}_{(r)}$ represents the value from the first estimate. With several iterations, we can get a stable solution for $\beta^{A}_{(r)}$. The number of iterations required for a stable solution depends on the range resolution of the signal. $\Delta\nu^{b}_{(r+\Delta r/2)}$ and $\Delta\nu^{e}_{(r+\Delta r/2)}$ can be approximated [36] as:

$$\Delta\nu^{b}_{(r+\Delta r/2)} \approx \frac{(4-\eta)\Delta\lambda}{2\Delta r\Delta\sigma_{O3}\lambda_{off}}\left(\frac{B_{(r)}}{1+B_{(r)}}-\frac{B_{(r+\Delta r)}}{1+B_{(r+\Delta r)}}\right), \tag{14}$$

$$\Delta\nu^{e}_{(r+\Delta r/2)} \approx -\frac{\Delta\lambda}{\Delta\sigma_{O3}\lambda_{off}}\left(\eta\alpha^{A}_{(r+\Delta r/2)}+4\alpha^{M}_{(r+\Delta r/2)}\right), \tag{15}$$

where η is the Ångström exponent, $\Delta\lambda$ is the wavelength separation, and $B_{(r)}$ is the aerosol-to-molecular backscatter ratio at the off-line wavelength defined as:

$$B_{(r)} = \beta^{A}_{(r)}/\beta^{M}_{(r)} \ . \tag{16}$$

Then, the ozone retrieval after the aerosol correction substituted into Eq. (11) recalculates the aerosol profile at the off-line wavelength.

The lidar ratio (S) exhibits a wide range of variation with different aerosol refractive indices, size distributions, and humidity. The S measurements have been made most frequently at 308 nm [66] and 355 nm [67-69]. The S for our DIAL wavelengths was assumed to be 40 sr^{-1} constant over the measurement range. The Ångström exponent (η) is often seen as an indicator of aerosol particle size: values greater than 2 correspond to large particles like sea salt and dust, and values smaller than 2 correspond to small smoke particles. Most of the reported η for tropospheric aerosol are measured at wavelengths longer than 300 nm with a variation from 0 to 2 [70, 71]. Considering η could be relatively small when it is applied in the UV region, we assume $\eta = 0.5$ at our DIAL wavelengths for urban aerosols [72].

Figure 5 shows the assumed aerosol, molecular, and ozone extinction profiles at 291 nm used in a model calculation to investigate the aerosol correction in the DIAL retrieval under an extremely large aerosol gradient condition. The hypothetical aerosol profile includes three basic regimes: homogeneous, increasing, and decreasing extinction. The aerosol extinction coefficients are arbitrarily set equal to zero below 1.2 km to investigate the downward propagating error. The molecular extinction profile derives from the 1976 U.S. Standard Atmosphere [73]. The hypothetic ozone contains a constant number density of $1.5\times10^{12}\,\mathrm{molec}\cdot\mathrm{cm}^{-3}$ and an absorption cross-section of $1.24\times10^{-18}\,\mathrm{cm}^{2}\cdot\mathrm{molec}^{-1}$ at 291 nm.

Figure 6 shows the comparison of the ozone retrieval both with and without aerosol correction as well as the calculated aerosol profile at 291 nm. This example calculation assumes that $\eta = 0.5$ and S=40 sr^{-1} are known exactly, and there is no signal measurement error. With a range resolution of 150 m, two total iterations from Eq. (11) to (15) produce the final aerosol-corrected ozone retrieval. In the process of calculating the aerosol profile, 10 iterations of Eq. (11) and (13) produces a stable aerosol solution. The derived aerosol backscatter is slightly lower than the model at the lower altitudes in the homogeneous aerosol region. This bias, in turn, produces a slightly higher ozone retrieval in the corresponding region. The aerosol-correction procedure reduces the retrieval errors from $\pm60\%$ to about $\pm5\%$. The residual errors are due to the numerical integration and the approximation of Eq. (14) and (15). The quality of this iterative procedure depends on the choice of S and h. According to Eq. (11), (14), and (15), S affects the aerosol profile retrieval while h affects only the final ozone correction.

Figure 7 shows the sensitivity test for S and h in the aerosol correction assuming that S=40 and $h = 0.5$ are the correct values. Inaccurate estimates of S or h can yield retrieval errors up to about 20%. Larger h will overestimate $\mathrm{D}n^{e}$, which produces less ozone and vice versa. h has a smaller impact on $\mathrm{D}n^{b}$ relative to $\mathrm{D}n^{e}$ due to the $4-h$ factor. The impact of S is larger in the inhomogeneous aerosol layer than in the homogeneous layer. The peak error is larger for underestimated S relative to overestimated S [74].

We summarize the iterative procedure as follows:

1. Calculate the first estimate of the ozone concentration from Eq. (3);
2. Substitute the first estimated ozone into the Eq. (11) to derive the aerosol backscatter profile for the off-line wavelength and iterate to obtain a stable solution with Eq. (13);
3. Calculate the differential aerosol backscatter and extinction corrections to obtain an second estimate ozone using Eq. (14) and (15);
4. With the second ozone estimate, go back to step 2.

4. Measurements

Figure 8 shows an ozone DIAL retrieval for 12 consecutive hours from 12:56 local time, Aug. 9 to 03:45, Aug. 10, 2008 with 10-min temporal integration (12000 shots) and 750-m vertical range resolution using the data processing described in the previous section. The aerosol time-height curtain (Figure 8a) exhibits moderate aerosol activity below 2 km with expected diurnal PBL variation and shorter time-scale fluctuations due to PBL processes. The maximum aerosol correction in Figure 8b corresponds to an ozone adjustment of 3-4 ppbv and occurs between 1.5 and 2.5 km for the largest vertical backscatter gradient. There was a short duration cloud at 2 km at 14:00. The retrievals for the two altitude channels overlap between 3.3 and 4.4 km to produce the final ozone profiles (Figure 8c) that agree well with the co-located ozonesonde (EN-SCI model 2Z with unbuffered 2% cathode solution) launched at 13:49 local time. The time-height curtain of ozone's evolution shows a very interesting structure of multiple ozone layers in the lower atmosphere that varies with time. One can see the buildup and decay of various layers throughout this 12-hour period. The high-frequency variation in the high-altitude channel (≥ 6 km) results partly from lower SNR and higher uncertainty of the SIB correction, both of which increase with altitude. Figure 9 shows the mean ozone profile and 1-sigma standard deviation for all the 10-min vertical profiles in Figure 8 as well as the coincident ozonesonde measurement. The high-altitude channel has a standard deviation increasing with altitude due to the statistical error distribution. Its standard deviation is less than 13 ppbv below 8 km and increases to about 45 ppbv at 8.5 km where the 285 laser does not have sufficient SNR for ozone retrieval; therefore, we terminate the retrievals at 8 km in Figure 8. The standard deviation of the low-altitude channel retrievals is less than 5 ppbv below 4 km and reaches 8 ppbv at 5 km due to lower SNR. The standard deviation at 2 km is a little larger than the surrounding altitudes possibly because of larger ozone fluctuation related to the PBL top. The two altitude channels have consistent mean retrievals in the overlap region with discrepancies less than 5 ppbv and similar standard deviations at 3.3 km which most likely reflect the true ozone short-term variation considering the physically credible structure in Figure 8. The mean retrievals agree with the ozonesonde measurement within about 10 ppbv and have higher biases at the upper altitudes.

5. Error Analysis

We divide the error budget of the DIAL retrieval into four categories: 1) Statistical uncertainties, ε_1, arising from signal and background noise fluctuations; 2) Errors, ε_2, associated with differential backscatter and extinction of non-ozone gases (O_2, SO_2, NO_2, etc.) and aerosols; 3) Errors, ε_3, due to uncertainties in the ozone absorption cross-section; and 4) Errors, ε_4, related to instrumentation and electronics. ε_1 is a random error; ε_2, ε_3, and ε_4 are systematic errors.

ε_1 can be written as [38]:

$$\varepsilon_1 = \frac{1}{2n\Delta r\Delta\sigma_{O3}}\sqrt{\sum_{j,\lambda}\frac{1}{(SNR_{j,\lambda})^2}}\,. \tag{11}$$

With the assumption of a Poisson distribution governing photon counting, the SNR at wavelength λ and range registration j becomes:

$$SNR_{j,\lambda} = \frac{P_{j,\lambda}}{P_{j,\lambda}{}^{1/2} + P_b + P_d} \tag{12}$$

where P_b is solar background counts, and P_d is dark counts. It is straightforward to show that ε_1 is proportional to $(\Delta r^3 NAP_L)^{-1/2}$, where N represents the total number of shots, A is the unobscured area of the telescope's primary mirror, and P_L is the number of the emitted laser photons. Δr must be chosen large enough to produce an acceptably small error. Figure 10 shows the estimated statistical errors for the high-altitude and low-altitude channels for a 10-min integration and 750-m range resolution. ε_1 is typically less than 10% below 4 km for our low-altitude channel and could be 20% at 5 km. This altitude performance gives us sufficient overlap for the two altitude channels under most atmospheric conditions. In the high-altitude channel, ε_1 exceeds 25% of the retrieval ozone near 8 ± 1 km, at which error altitude we terminate the retrieval.

ε_2 includes the interference from O_2, SO_2, NO_2, air molecules, and aerosols. Table 2 summaries the potential errors in the DIAL retrieval for 285 and 291 nm wavelengths due to non-ozone absorption gases. The calculation of the oxygen dimer (O_2-O_2) interference includes some uncertainties due to the absorption cross-section measurement. The O_2-O_2 absorption theory has not been entirely established [75]. The local SO_2 and NO_2 profiling data are not available. However, the estimated error due to either SO_2 or NO_2 using the latest ground observation is less than 1%. The impact caused by differential Rayleigh extinction results in an inaccuracy of less than 1% using balloon ozonesonde retrievals of atmospheric density or by employing climatological models.

The main concern comes from the aerosol interference, which depends on both the wavelengths and wavelength separation. Although the aerosol optical properties could be retrieved from a third wavelength, the differential effect for a DIAL wavelength pair still has some uncertainty due to the assumption for lidar ratio and Ångström exponent. Within the PBL, where the statistical errors are small, differential aerosol backscattering and extinction dominate the error sources [36, 38, 40]. However, it is reasonable to believe that the error due to aerosol interference is smaller than 20% after the aerosol correction as shown in section 3.4.

The uncertainty in the Bass-Paur ozone cross-sections is believed to be less than 2% [75-77]. ε_3 will be less than 3% after considering the temperature dependence.

ε_4 could be caused by a misalignment of the lasers with the telescope FOV, imperfect dead-time, or SIB correction. Dead time distorts the near-range signal, and SIB distorts the far-range signal. Because the dead-time behavior is reliably characterized, the error caused by SIB usually is larger than the dead-time error. For the 10-min integration data, ε_4 is believed to be <5% at 1-4 km for our low-altitude channel and <10% for our high-altitude channel below 8 km based on the LED test results and the analysis of our previous data such as Figure 8 and 9. A summary of the errors in the DIAL measurements appears on Table 3 for a constant tropospheric ozone of 60-ppbv, 750-m vertical resolution, and 10-min integration.

Figure 11 shows a comparison of 12 lidar retrievals and their single coincident ozonesonde measurement between 1300 and 1400 local time except for the first profile on Aug. 17, 2008 (upper right panel), which was taken at 0800. The aerosol correction was made at altitudes between 1 and 3 km. Figure 12 shows the mean percentage differences and their standard errors of the mean for all those retrievals. The lidar retrievals of the low-altitude channel agree with ozonesonde measurements within 10% from 1 to 4 km. The relatively high errors at about 2 km possibly relate to residual aerosol correction errors around PBL height. The lidar retrievals from the high-altitude channel agree with ozonesonde to within 20% below 8 km. The statistical error and the uncertainty associated with the SIB correction result in larger errors for the high-altitude channel above 6 km.

6. Conclusion and Future Plans

The RAPCD ozone DIAL system measures tropospheric ozone profiles during both daytime and nighttime using the 285/291-nm wavelength pair. The low-altitude receiving channel makes ozone measurements at altitudes between 1-5 km using a 10-cm telescope and Hamamatsu R7400U PMTs. The high-altitude channel measures ozone between 3 and about 8 km using a 40-cm telescope and EMI 9813 PMTs. Model calculations demonstrate that the iterative aerosol correction procedure significantly reduces the retrieval error arising from differential aerosol backscatter in the lower troposphere where the quality of the aerosol correction depends on the accuracy of the a priori lidar ratio and Ångström exponent. A comparison of the lidar retrievals and coincident ozonesonde measurements suggest that retrieval accuracy ranges from better than 10% after the application of an aerosol correction below 4 km to better than 20% for altitudes below 8 km with 750-m vertical resolution and 10-min integration. Error sources include statistical uncertainty, differential scattering and absorption from non-ozone species, uncertainty in ozone absorption cross-section, and imperfection of the dead-time and SIB corrections. The uncertainty in the SIB correction and the statistical errors dominate the error sources in the free troposphere and could be reduced by increasing the integration time or reducing the range resolution.

Future improvements will overcome two major limitations of the current system by: 1) extending observations into upper troposphere by replacing the current transmitters with more powerful ones and shifting the current wavelengths to longer ones to make higher-altitude nighttime measurements; 2) Minimizing aerosol interference in the lower troposphere by adding a third wavelength (dual-DIAL technique). This lidar with expected improvements will provide a unique dataset to investigate the chemical and dynamical processes in the PBL and free-troposphere. The spatio-temporal variance estimates derived from the ozone lidar observations will also be useful for assessing the variance of tropospheric ozone captured by satellite retrievals.

Acknowledgements

The authors would like to thank Tom McGee, Stuart McDermid, and Thierry Leblanc for extensive discussions, Jack Kaye, P. K. Bhartia, and Rich McPeters for continuing support and to thank the UAHuntsville ozonesonde team: Rochelle Williams, Patrick Buckley, and Danielle Nuding for providing the ozonesonde data. They also thank Whitney Guerin for editing the manuscript.

References

[1] D. Shindell, G. Faluvegi, A. Lacis, J. Hansen, R. Ruedy, and E. Aguilar, "Role of tropospheric ozone increases in 20th-century climate change," *J. Geophys. Res.,* 111, p. D08302, 2006.

[2] J. Lelieveld and F. J. Dentener, "What controls tropospheric ozone?," *J. Geophys. Res.,* 105, pp. 3531-3551, February 2000.

[3] J. Stutz, B. Alicke, R. Ackermann, A. Geyer, A. White, and E. Williams, "Vertical profiles of NO_3, N_2O_5, O_3, and NO_x in the nocturnal boundary layer: 1. Observations during the Texas Air Quality Study 2000," *J. Geophys. Res.,* 109, p. D12306, 2004.

[4] A. Geyer and J. Stutz, "Vertical profiles of NO_3, N_2O_5, O_3, and NOx in the nocturnal boundary layer: 2. Model studies on the altitude dependence of composition and chemistry," *J. Geophys. Res.,* 109, p. D12307, Correction published 18 August 2004. 2004.

[5] J. Liang, L. W. Horowitz, D. J. Jacob, Y. Wang, A. M. Fiore, J. A. Logan, G. M. Gardner, and J. W. Munger, "Seasonal budgets of reactive nitrogen species and ozone over the United States, and export fluxes to the global atmosphere," *J. Geophys. Res.,* 103, pp. 13,435-13,450, June 1998.

[6] W. B. Grant, E. V. Browell, C. F. Butler, M. A. Fenn, M. B. Clyton, J. R. Hannan, H. E. Fuelberg, D. R. Blake, N. J. Blake, G. L. Gregory, B. G. Heikes, G. W. Sachse, H. B. Singh, J. Snow, and R. W. Talbot, "A case study of transport of tropical marine boundary layer

and lower tropospheric air masses to the northern midlatitude upper troposphere," *J. Geophys. Res.,* 105, pp. 3757-3769, February 2000.

[7] H. Eisele, H. E. Scheel, R. Sladkovic, and T. Trickl, "High-resolution lidar measurements of stratosphere-troposphere exchange," *J. Atmos. Sci.,* 56, pp. 319-330, January 1999.

[8] A. Stohl, P. Bonasoni, P. Cristofanelli, W. Collins, J. Feichter, A. Frank, C. Forster, E. Gerasopoulos, H. Gäggeler, P. James, T. Kentarchos, H. Kromp-Kolb, B. Krüger, C. Land, J. Meloen, A. Papayannis, A. Priller, P. Seibert, M. Sprenger, G. J. Roelofs, H. E. Scheel, C. Schnabel, P. Siegmund, L. Tobler, T. Trickl, H. Wernli, V. Wirth, P. Zanis, and C. Zerefos, "Stratosphere-troposphere exchange: A review and what we learned from STACCATO," *J. Geophys. Res.,* 108, p. 8516, 2003.

[9] A. O. Langford, C. D. Masters, M. H. Proffitt, E.-Y. Hsie, and A. F. Tuck, "Ozone measurements in a tropopause fold associated with a cut-off low system," *Geophys. Res. Lett.,* 23, pp. 2501-2504, 1996.

[10] A. J. DeCaria, K. E. Pickering, G. L. Stenchikov, and L. E. Ott, "Lightning-generated NO_x and its impact on tropospheric ozone production: A three-dimensional modeling study of a Stratosphere-Troposphere Experiment: Radiation, Aerosols and Ozone (STERAO-A) thunderstorm," *J. Geophys. Res.,* 110, p. D14303, 2005.

[11] O. R. Cooper, A. Stohl, M. Trainer, A. M. Thompson, J. C. Witte, S. J. Oltmans, G. Morris, K. E. Pickering, J. H. Crawford, G. Chen, R. C. Cohen, T. H. Bertram, P. Wooldridge, A. Perring, W. H. Brune, J. Merrill, J. L. Moody, D. Tarasick, P. Nédélec, G. Forbes, M. J. Newchurch, F. J. Schmidlin, B. J. Johnson, S. Turquety, S. L. Baughcum, X. Ren, F. C.

Fehsenfeld, J. F. Meagher, N. Spichtinger, C. C. Brown, S. A. McKeen, I. S. McDermid, and T. Leblanc, "Large upper tropospheric ozone enhancements above midlatitude North America during summer: In situ evidence from the IONS and MOZAIC ozone measurement network," *J. Geophys. Res.,* 111, 2006.

[12] O. R. Cooper, M. Trainer, A. M. Thompson, S. J. Oltmans, D. W. Tarasick, J. C. Witte, A. Stohl, S. Eckhardt, J. Lelieveld, M. J. Newchurch, B. J. Johnson, R. W. Portmann, L. Kalnajs, M. K. Dubey, T. Leblanc, I. S. McDermid, G. Forbes, D. Wolfe, T. Carey-Smith, G. A. Morris, B. Lefer, B. Rappenglück, E. Joseph, F. Schmidlin, J. Meagher, F. C. Fehsenfeld, T. J. Keating, R. A. V. Curen, and K. Minschwaner, "Evidence for a recurring eastern North America upper tropospheric ozone maximum during summer," *J. Geophys. Res.,* 112, p. D23304, 2007.

[13] U. Schumann and H. Huntrieser, "The global lightning-induced nitrogen oxides source," *Atmos. Chem. Phys.,* 7, pp. 3823-3907, 2007.

[14] S. J. Oltmans, H. Levy II, J. M. Harris, J. T. Merrill, J. L. Moody, J. A. Lathrop, E. Cuevas, M. Trainer, M. S. O'Neill, J. M. Prospero, H. Vömel, and B. J. Johnson, "Summer and spring ozone profiles over the North Atlantic from ozonesonde measurements," *J. Geophys. Res.,* 101, pp. 29,179-29,200, December 1996.

[15] M. J. Newchurch, M. A. Ayoub, S. Oltmans, B. Johnson, and F. J. Schmidlin, "Vertical distribution of ozone at four sites in the United States," *J. Geophys. Res.,* 108, p. 4031, 15 January 2003.

[16] R. D. McPeters, G. J. Labow, and B. J. Johnson, "A satellite-derived ozone climatology for

balloonsonde estimation of total column ozone," *J. Geophys. Res.,* 102, pp. 8875-8885, April 1997.

[17] J. P. Burrows, M. Weber, M. Buchwitz, V. Rozanov, A. Ladstätter-Weißenmayer, A. Richter, R. DeBeek, R. Hoogen, K. Bramstedt, K.-U. Eichmann, and M. Eisinger, "The Global Ozone Monitoring Experiment (GOME): Mission concept and first scientific results," *J. Atmos. Sci.,* 56, pp. 151-175, January 1999.

[18] M. J. Newchurch, D. M. Cunnold, and J. Cao, "Intercomparison of Stratospheric Aerosol and Gas Experiment (SAGE) with Umkehr[64] and Umkehr[92] ozone profiles and time series: 1979-1991," *J. Geophys. Res.,* 103, pp. 31,277-31,292, December 1998.

[19] M. J. Newchurch, E. S. Yang, D. M. Cunnold, G. C. Reinsel, J. M. Zawodny, and J. M. R. III, "Evidence for slowdown in stratospheric ozone loss: First stage of ozone recovery," *J. Geophys. Res.,* 108, p. 4507, 23 August 2003.

[20] J. M. Russell III, L. L. Gordley, J. H. Park, S. R. Drayson, W. D. Hesketh, R. J. Cicerone, A. F. Tuck, J. E. Frederick, J. E. Harries, and P. J. Crutzen, "The Halogen Occultation Experiment," *J. Geophys. Res.,* 98, pp. 10,777-10,797, June 1993.

[21] J. W. Waters, L. Froidevaux, G. L. Manney, W. G. Read, and L. S. Elson, "MLS observations of lower stratospheric ClO and O3 in the 1992 southern hemisphere winter," *Geophys. Res. Lett.,* 20, pp. 1219-1222, 1993.

[22] X. Liu, K. Chance, C. E. Sioris, R. J. D. Spurr, T. P. Kurosu, R. V. Martin, and M. J. Newchurch, "Ozone profile and tropospheric ozone retrievals from Global Ozone Monitoring Experiment: Algorithm description and validation," *J. Geophys. Res.,* 110, p.

D20307, 2005.

[23] J. R. Ziemke, S. Chandra, B. N. Duncan, L. Froidevaux, P. K. Bhartia, P. F. Levelt, and J. W. Waters, "Tropospheric ozone determined from Aura OMI and MLS: Evaluation of measurements and comparison with the Global Modeling Initiative's Chemical Transport Model," *J. Geophys. Res.,* 111, p. D19303, 2006.

[24] Y. Choi, Y. Wang, T. Zeng, D. Cunnold, E.-S. Yang, R. Martin, K. Chance, V. Thouret, and E. Edgerton, "Springtime transitions of NO_2, CO, and O_3 over North America: Model evaluation and analysis," *J. Geophys. Res.,* 113, p. D20311, 2008.

[25] Q. Yang, D. M. Cunnold, H.-J. Wang, L. Froidevaux, H. Claude, J. Merrill, M. Newchurch, and S. J. Oltmans, "Midlatitude tropospheric ozone columns derived from the Aura Ozone Monitoring Instrument and Microwave Limb Sounder measurements," *J. Geophys. Res.,* 112, pp. D20305, doi:10.1029/2007JD008528, 2007.

[26] J. H. Kim, M. J. Newchurch, and K. Han, "Distribution of tropical tropospheric ozone determined by the scan-angle method applied to TOMS measurements," *J. Atmos. Sci.,* 58, pp. 2699-2708, June 2001.

[27] J. H. Kim and M. J. Newchurch, "Biomass-burning influence on tropospheric ozone over New Guinea and South America," *J. Geophys. Res.,* 103, pp. 1455-1461, January 1998.

[28] J. H. Kim, S. Na, M. J. Newchurch, and R. V. Martin, "Tropical tropospheric ozone morphology and seasonality seen in satellite and in situ measurements and model calculations," *J. Geophys. Res.,* 110, p. D02303, 2005.

[29] X. Liu, K. Chance, C. E. Sioris, T. P. Kurosu, R. Spurr, R. V. Martin, T. Fu, J. Logan, D. Jacob, P. Palmer, M. J. Newchurch, I. A. Megretskaia, and R. B. Chatfield, "First directly retrieved global distribution of tropospheric column ozone from GOME: Comparison with the GEOS-CHEM model," *J. Geophys. Res.,* 111, p. D02308, 2006 2006.

[30] X. Liu, K. Chance, C. E. Sioris, T. P. Kurosu, and M. J. Newchurch, "Intercomparison of GOME, ozonesonde, and SAGE II measurements of ozone: Demonstration of the need to homogenize available ozonesonde data sets," *J. Geophys. Res.,* 111, p. D14305, 2006.

[31] W. Steinbrecht, T. J. McGee, L. W. Twigg, H. Claude, F. Schönenborn, G. K. Sumnicht, and D. Silbert, "Intercomparison of stratospheric ozone and temperature profiles during the October 2005 Hohenpeißenberg Ozone Profiling Experiment (HOPE)," *Atmos. Meas. Tech.,* 2, pp. 125-145, 2009.

[32] T. Trickl, N. Bärtsch-Ritter, H. Eisele, M. Furger, R. Mücke, and A. Stohl, "High-ozone layers in the middle and upper troposphere above Central Europe: strong import from the stratosphere over the Pacific Ocean," *Atmos. Chem. Phys. Discuss.,* 9, pp. 3113-3166, 2009.

[33] Y. Zhao, R. D. Marchbanks, and R. M. Hardesty, "ETL's Transportable Lower Troposphere Ozone Lidar and Its Applications in Air Quality Studies," in *Proc. SPIE 3127*, 1997, pp. 53-62.

[34] R. J. Alvarez II, W. A. Brewer, D. C. Law, J. L. Machol, R. D. Marchbanks, S. P. Sandberg, C. J. Senff, and A. M. Weickmann, "Development and application of the TOPAZ airborne lidar system by the NOAA Earth System Research Laboratory," in *24th International*

Laser Radar Conference, 2008, pp. 68-71.

[35] G. Ancellet, A. Papayannis, J. Pelon, and G. Mégie, "DIAL tropospheric ozone measurement using a Nd:YAG laser and the Raman shifting technique," *J. Atmos. Oceanic Technol.,* 6, pp. 832–839, 1989.

[36] E. V. Browell, S. Ismail, and S. T. Shipley, "Ultraviolet DIAL measurements of O_3 profiles in regions of spatially inhomogeneous aerosols," *Appl. Opt.*, 24, pp. 2827-2836, September 1985.

[37] T. Fukuchi, T. Fujii, N. Cao, and K. Nemoto, "Tropospheric O_3 measurements by simultaneous differential absorption lidar and null profiling," *Opt. Eng.,* 40, pp. 1944-1949, 2001.

[38] A. Papayannis, G. Ancellet, J. Pelon, and G. Mégie, "Multiwavelength lidar for ozone measurements in the troposphere and the lower stratosphere," *Appl. Opt.,* 29, pp. 467-476, February 1990.

[39] M. H. Proffitt and A. O. Langford, "Ground-based differential absorption lidar system for day or night measurements of ozone throughout the free troposphere," *Appl. Opt.,* 36, pp. 2568-2585, April 1997.

[40] J. A. Sunesson, A. Apituley, and D. P. J. Swart, "Differential absorption lidar system for routine monitoring of tropospheric ozone," *Appl. Opt.,* 33, pp. 7045-7058, October 1994.

[41] I. S. McDermid, D. A. Haner, M. M. Kleiman, T. D. Walsh, and M. L. White, "Differential absorption lidar system for tropospheric and stratospheric ozone measurements," *Opt. Eng.,*

30, pp. 22-30, 1991.

[42] T. J. McGee, M. R. Gross, U. N. Singh, J. J. Butler, and P. E. Kimvilakani, "Improved stratospheric ozone lidar," *Opt. Eng.*, 34, pp. 1421-1430, May 1995.

[43] J. Pelon, S. Godin, and G. Mégie, "Upper stratospheric (30-50 km) lidar observations of the ozone vertical distribution," *J. Geophys. Res.*, 91, pp. 8667-8671, 1986.

[44] O. Uchino and I. Tabata, "Mobile lidar for simultaneous measurements of ozone, aerosols, and temperature in the stratosphere," *Appl. Opt.*, 30, pp. 2005-2012, May 1991.

[45] E. V. Browell, S. Ismail, and W. B. Grant, "Differential absorption lidar (DIAL) measurements from air and space," *Appl. Phys.*, B67, pp. 399-410, 1998.

[46] O. R. Cooper, A. Stohl, S. Eckhardt, D. D. Parrish, S. J. Oltmans, B. J. Johnson, P. Nédélec, F. J. Schmidlin, M. J. Newchurch, Y. Kondo, and K. Kita, "A springtime comparison of tropospheric ozone and transport pathways on the east and west coasts of the United States," *J. Geophys. Res.*, 110, p. D05S90, 2005 2005.

[47] G. J. Megie, G. Ancellet, and J. Pelon, "Lidar measurements of ozone vertical profiles," *Appl. Opt.*, 24, pp. 3454-3463, 1985.

[48] A. E. Siegman, *Standard for the Measurement of Beam Widths, Beam Divergence, and Propagation Factors, Proposal for a Working Draft*: ISO, 1991.

[49] J. Burris, W. Heaps, B. Gary, W. Hoegy, L. Lait, T. McGee, M. Gross, and U. Singh, "Lidar temperature measurements during the Tropical Ozone Transport Experiment (TOTE)/Vortex Ozone Transport Experiment (VOTE) mission," *J. Geophys. Res.*, 103, pp.

3505-3510, 1998.

[50] J. Burris, T. McGee, W. Hoegy, P. Newman, L. Lait, L. Twigg, G. Sumnicht, W. Heaps, C. Hostetler, R. Neuber, and K. F. Künzi, "Lidar temperature measurements during the SOLVE campaign and the absence of polar stratospheric clouds from regions of very cold air," *J. Geophys. Res.,* 107, p. 8297, 2002.

[51] D. P. Donovan, J. A. Whiteway, and A. I. Carswell, "Correction for nonlinear photon-counting effects in lidar systems," *Appl. Opt.,* 32, pp. 6742-6753, 1993.

[52] M. Lampton and J. Bixler, "Counting efficiency of systems having both paralyzable and nonparalyzable elements," *Rev. Sci. Instrum.,* 56 pp. 164-165, January 1985.

[53] D. N. Whiteman, B. Demoz, P. D. Girolamo, J. Comer, I. Veselovskii, K. Evans, Z. Wang, M. Cadirola, K. Rush, G. Schwemmer, B. Gentry, S. H. Melfi, B. Mielke, D. Venable, and T. V. Hove, "Raman lidar measurements during the International H_2O Project. Part I: Instrumentation and analysis techniques," *J. Atmos. Oceanic Technol.,* 23, pp. 157-169, 2006.

[54] R. Newsome, D. Turner, M. Clayton, and R. Ferrare, "Progress on the use of combined analog and photon counting detection for Raman lidar," in *Proceeding of 24th International Laser Radar Conference, Volume I*, 2008, pp. 185-188.

[55] Burle, "Photomultiplier Handbook," pp. 56-57, 1989.

[56] F. Cairo, F. Congeduti, M. Poli, S. Centurioni, and G. D. Donfrancesco, "A survey of the signal-induced noise in photomultiplier detection of wide dynamics luminous signals," *Rev.*

Sci. Instrum., 67, pp. 3274-3280, 1996.

[57] Y. Zhao, "Signal-induced fluorescence in photomultipliers in differential absorption lidar systems," *Appl. Opt.,* 38, pp. 4639-4648, 1999.

[58] T. J. McGee, R. A. Ferrare, D. N. Whiteman, J. J. Butler, J. F. Burris, and M. A. Owens, "Lidar measurements of stratospheric ozone during the STOIC campaign," *J. Geophys. Res.,* 100, pp. 9255-9262, 1995.

[59] M. R. Measures, *Laser remote sensing: Fundamentals and applications*. New York: John Wiley and Sons, Inc., 1984.

[60] V. A. Kovalev and W. E. Eichinger, *Elastic lidar theory, practice, and analysis methods*. New York: John Wiley and Sons, Inc., 2004.

[61] J. R. Taylor, *An Introduction to Error Analysis: The Study of Uncertainties in Physical Measurements*. Mill Valley, CA: Oxford University Press, 1982.

[62] F. Immler, "A new algorithm for simultaneous ozone and aerosol retrieval from tropospheric DIAL measurements," *Appl. Phys. B,* 76, pp. 593-596, 2003.

[63] Y. Sasano, "Simultaneous determination of aerosol and gas distribution by DIAL measurements," *Appl. Opt.,* 27, pp. 2640-2641, 1988.

[64] V. A. Kovalev and M. P. Bristow, "Compensational three-wavelength differential-absorption lidar technique for reducing the influence of differential scattering on ozone-concentration measurements," *Appl. Opt.,* 35, pp. 4790-4797, August 1996.

[65] Z. Wang, H. Nakane, H. Hu, and J. Zhou, "Three-wavelength dual differential absorption lidar method for stratospheric ozone measurements in the presence of volcanic aerosols," *Appl. Opt.,* 36, pp. 1245-1252, February 1997.

[66] A. Ansmann, M. Riebesell, U. Wandinger, C. Weitkamp, W. E. Voss, W. Lahmann, and W. Michaelis, "Combined Raman elastic-backscatter LIDAR for vertical profiling of moisture, aerosol extinction, backscatter, and LIDAR ratio," *Appl. Phys.,* B55, pp. 18-28, February 1992.

[67] J. Ackermann, "The extinction-to-backscatter ratio of tropospheric aerosol: A numerical study," *J. Atmos. Oceanic Technol.,* 15, pp. 1043-1050, 1998.

[68] R. Ferrare, S. Melfi, D. Whiteman, K. Evans, and R. Leifer, "Raman lidar measurements of aerosol extinction and backscattering 1. Methods and comparisons," *J. Geophys. Res.,* 103, pp. 19,663-19,672, 1998.

[69] D. Müller, A. Ansmann, I. Mattis, M. Tesche, U. Wandinger, D. Althausen, and G. Pisani, "Aerosol-type-dependent lidar ratios observed with Raman lidar," *J. Geophys. Res.,* 112, p. D16202, 2007.

[70] C. M. Carrico, M. H. Bergin, J. Xu, K. Baumann, and H. Maring, "Urban aerosol radiative properties: Measurements during the 1999 Atlanta Supersite Experiment," *J. Geophys. Res.,* 108, p. 8422, 2003.

[71] D. Müller, I. Mattis, U. Wandinger, A. Ansmann, D. Althausen, and A. Stohl, "Raman lidar observations of aged Siberian and Canadian forest fire smoke in the free troposphere over Germany in 2003: Microphysical particle characterization," *J. Geophys. Res.,* 110, p.

D17201, 2005.

[72] T. F. Eck, B. N. Holben, J. S. Reid, O. Dubovik, A. Smirnov, N. T. O'Neill, I. Slutsker, and S. Kinne, "Wavelength dependence of the optical depth of biomass burning, urban, and desert dust aerosols," *J. Geophys. Res.,* 104, pp. 31,333-31,349, 27 December 1999.

[73] NOAA, *U.S. Standard Atmosphere, 1976*: Government Printing Office, 1976.

[74] V. A. Kovalev, "Sensitivity of the lidar solution to errors of the aerosol backscatter-to-extinction ratio: influence of a monotonic change in the aerosol extinction coefficient," *Appl. Opt.,* 34, pp. 3457-3462, 1995.

[75] J. Orphal, "A critical review of the absorption cross-sections of O_3 and NO_2 in the 240-790 nm region," *J. Photochem. Photobiol., A,* 157, pp. 185-209, 2003.

[76] A. M. Bass and R. J. Paur, "Absorption cross-sections for ozone: the temperature dependence," *J. Photochem.,* 17, 1981.

[77] J. Orphal and K. Chance, "Ultraviolet and visible absorption cross-sections for HITRAN," *J. Quant. Spectrosc. Radiat. Trans.,* 82, pp. 491-504, 2003.

[78] A. S. Jursa, "Handbook of Geophysics and the Space Environment," Air Force Geophysics Laboratory, 1985.

[79] S. Fally , A. C. Vandaele, M. Carleer, C. Hermans, A. Jenouvrier, M.-F. Mérienne, B. Coquart, and R. Colin, "Fourier Transform Spectroscopy of the O_2 Herzberg bands. III. Absorption cross-sections of the collision-induced bands and of the Herzberg continuum," *J. Mol. Spectrosc.,* 204, pp. 10-20, 2000.

[80] J. Rufus, G. Stark, P. L. Smith, J. C. Pickering, and A. P. Thorne, "High-resolution photoabsorption cross section measurements of SO_2, 2: 220 to 325 nm at 295 K," *J. Geophys. Res.,* 108, p. 5011, 2003.

[81] Natural Resources and Environmental Management Division, "*Air quality report, data summaries, trend analysis and program activities (2001-2005)*," Huntsville, Alabama 2006.

[82] K. Bogumil, J. Orphal, T. Homann, S. Voigt, P. Spietz, O. C. Fleischmann, A. Vogel, M. Hartmann, H. Bovensmann, J. Frerick, and J. P. Burrows, "Measurements of molecular absorption spectra with the SCIAMACHY pre-flight model: instrument characterization and reference data for atmospheric remote-sensing in the 230–2380 nm region," *J. Photochem. Photobiol. A: Chem.,* 157, pp. 167–184, 2003.

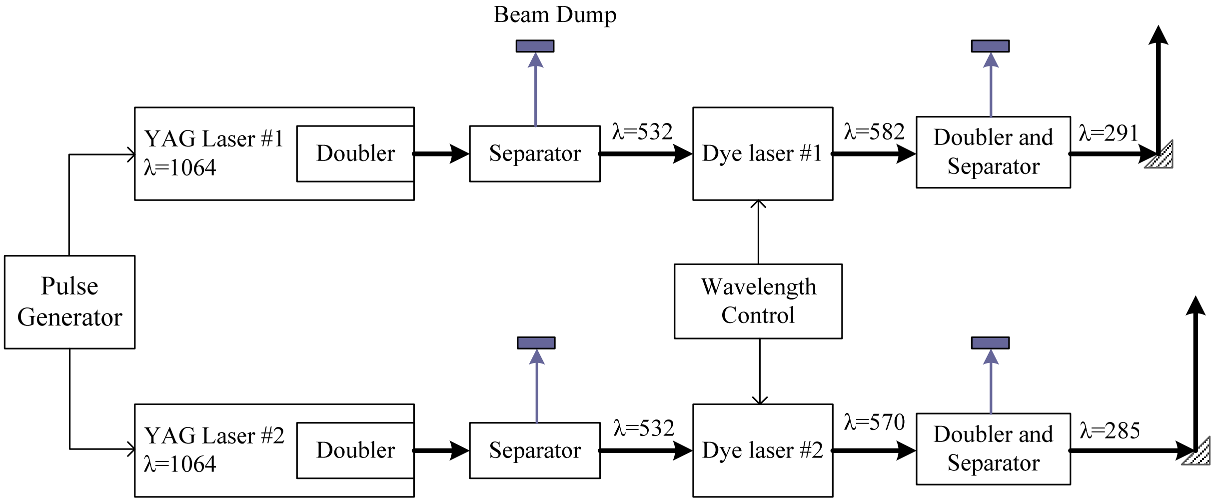

Figure 1. Transmitter diagram.

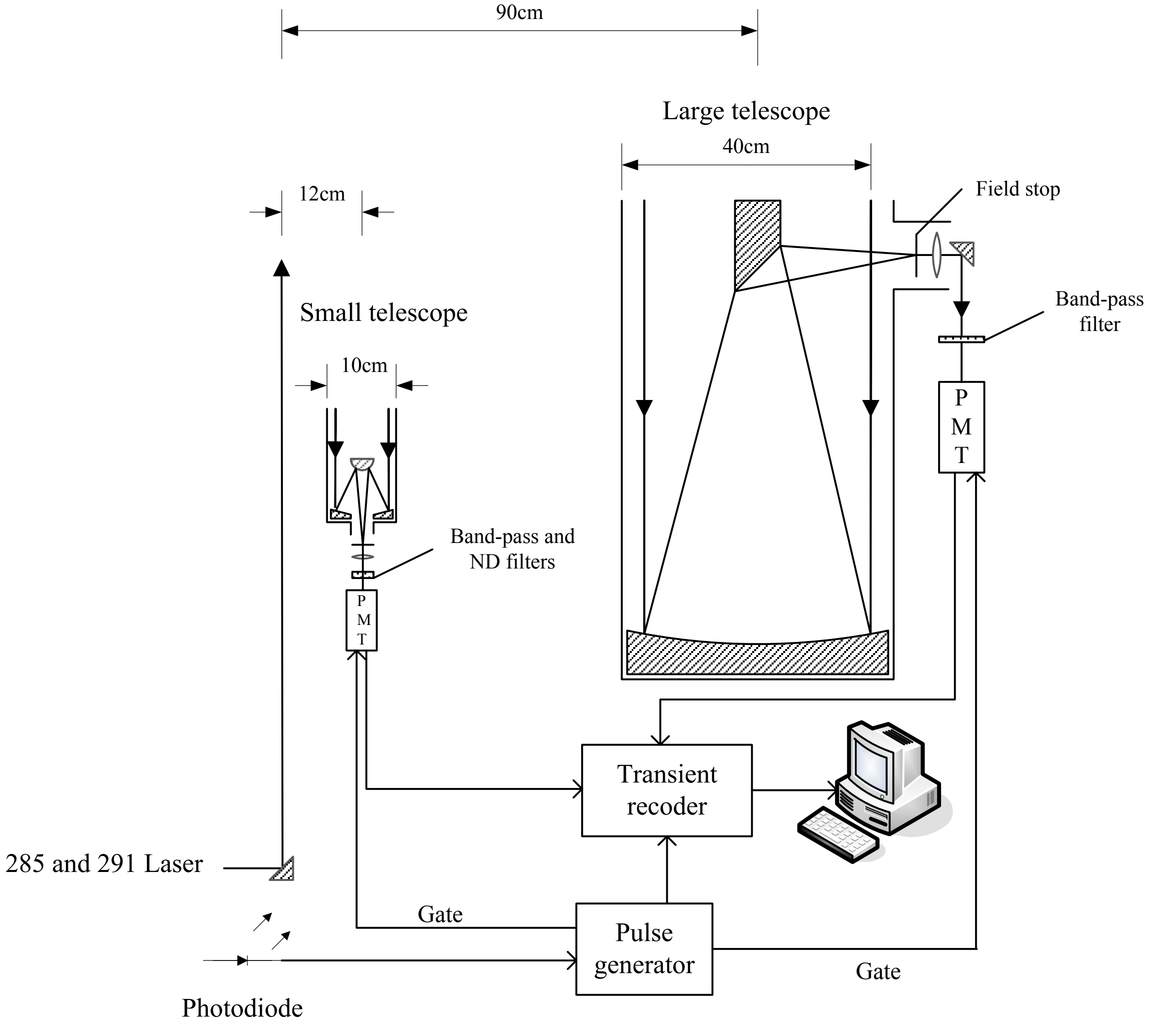

Figure 2. Diagram of the receivers and detectors.

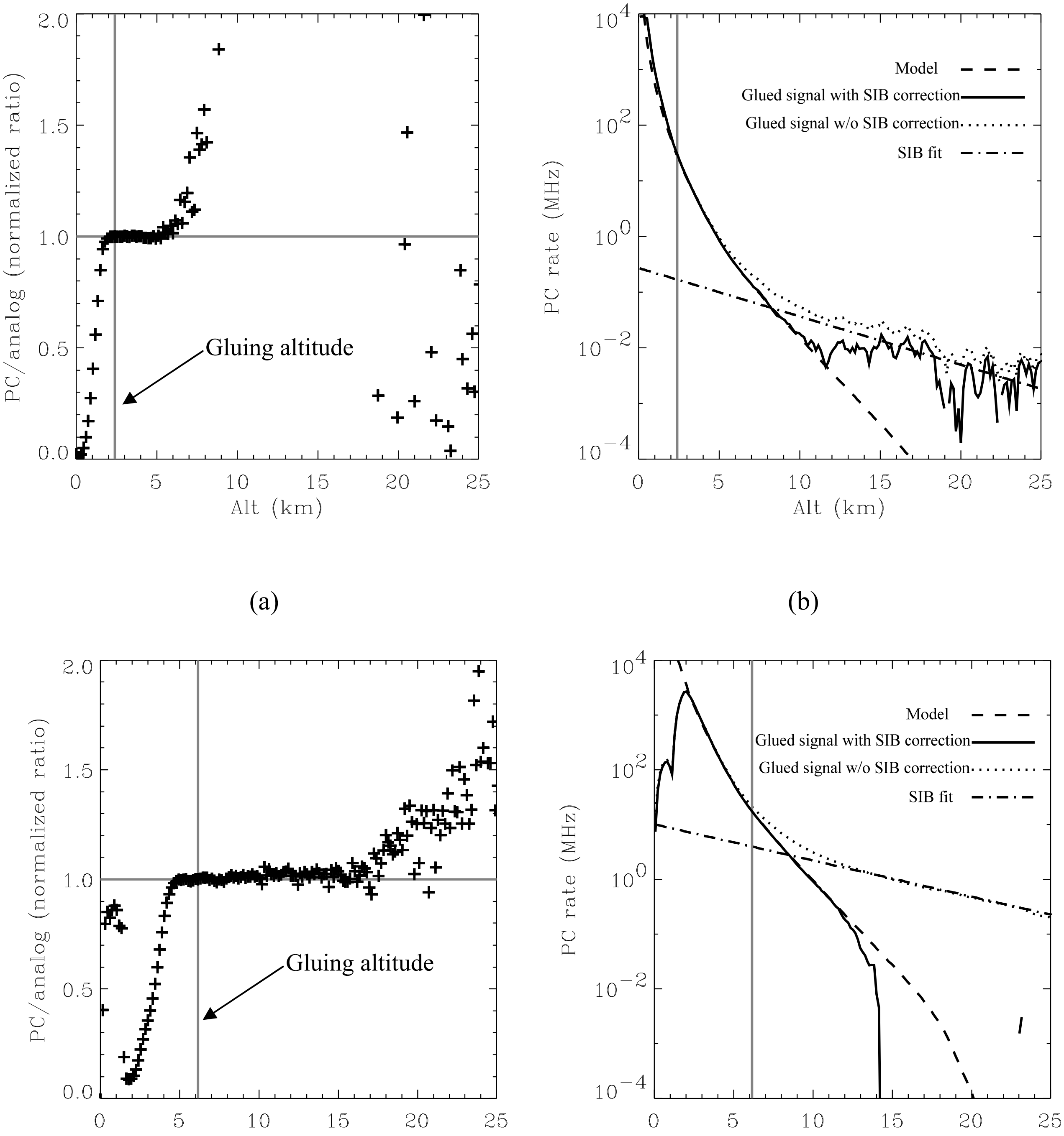

(a) (b)

(c) (d)

Figure 3. An example of gluing and SIB correction for 285-nm signal. The 10-min averaged data occured at 13:00 local time on Oct. 18, 2008. (a) The normalized ratio of photoncounting (PC) to analog after background and dead-time corrections for the low-altitude channel signal. (b)

Comparison of the non-SIB-corrected, SIB-corrected signal and model as well as the SIB fitting function for the low-altitude signal. The model uses the coincident ozonesonde measurement assuming no aerosol. The SIB fitting function ($\exp(-1.3 - alt \cdot 2 \cdot 10^{-1})$) uses previously retrieved data and coincident ozonesonde measurements. (c) Same as (a) but for the high-altitude channel. (d) Same as (b) but for the high-altitude channel. The coefficients of the SIB fitting function result from an empirical single exponential least-squares fit to the signal acquired from 100 to 160 μs after data acquisition starts.

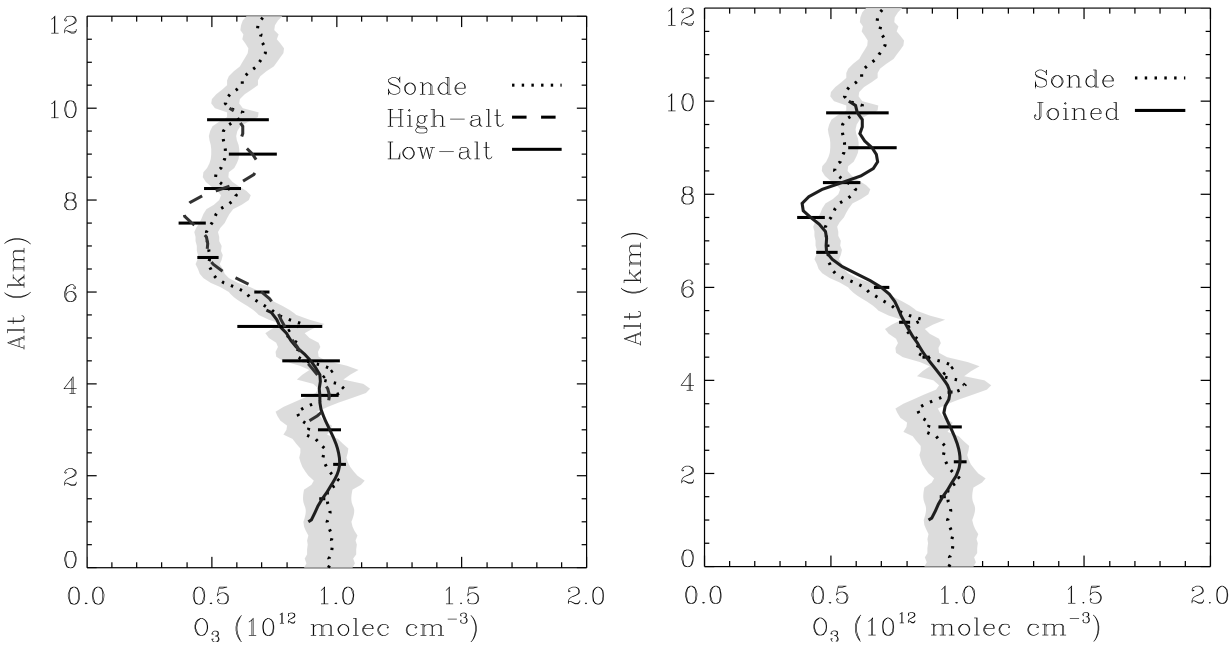

(a) (b)

Figure 4. An example of a joined ozone retrieval for the lidar data in Figure 3. (a) Separate retrievals of the two altitude channels. The error bars represent the 1-sigma statistical uncertainties. The gray envelope represents ±10% uncertainty of the coincident ozonesonde profile. (b) The joined DIAL retrieval from the two altitude channels and its combined 1-sigma statistical uncertainty.

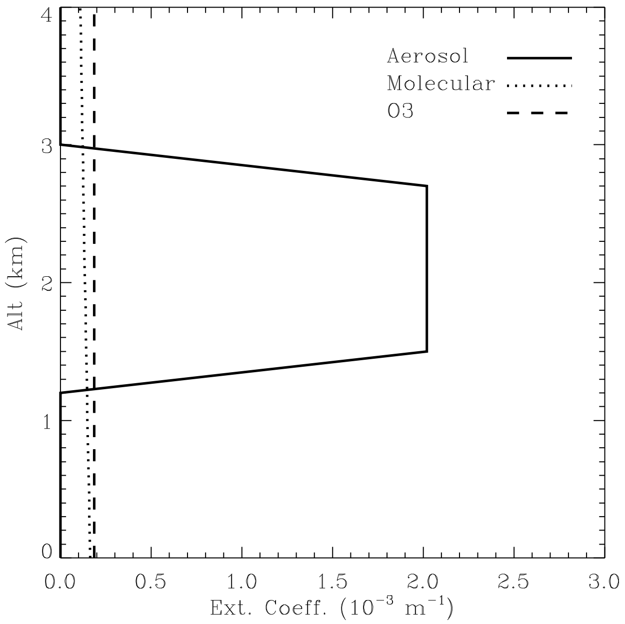

Figure 5. Aerosol, molecular, and ozone extinction coefficient profiles at 291 nm for a model calculation of extreme aerosol effects.

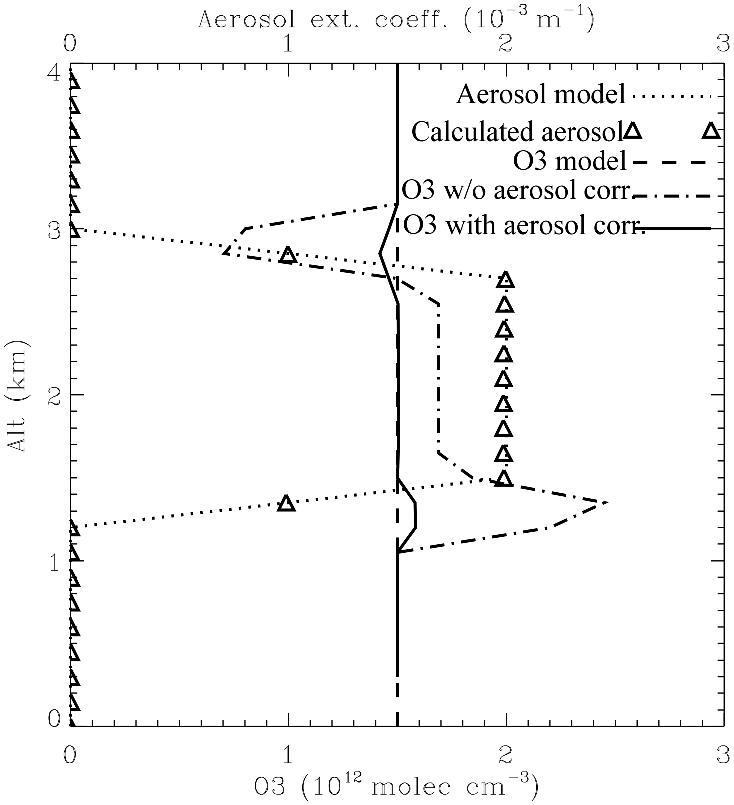

Figure 6. Comparison of the simulated ozone retrieval without aerosol correction against that with aerosol correction using the iterative procedure. The Ångström exponent (η) and lidar ratio (S) were assumed to be exactly known at 0.5 and 40 sr^{-1} respectively for the aerosol correction. The aerosol correction dramatically improves the ozone retrieval.

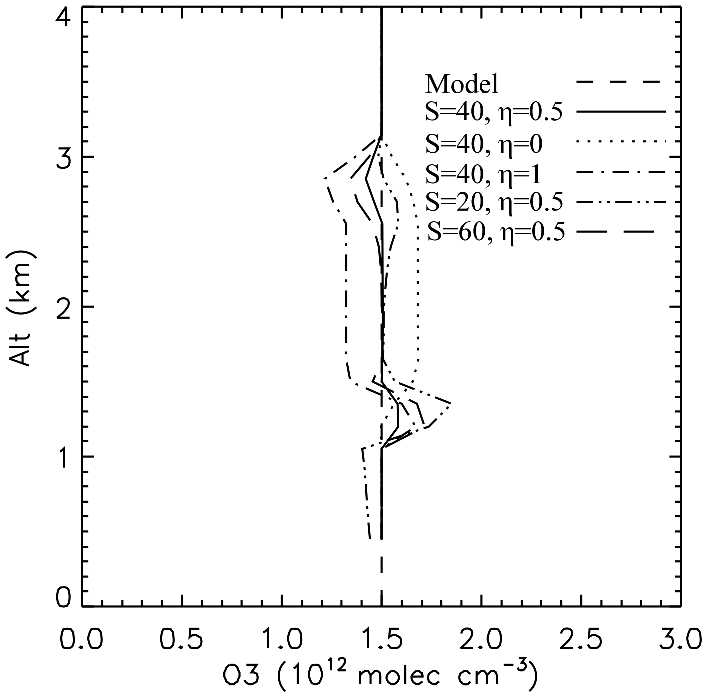

Figure 7. Ozone retrieval using different Ångström exponents ($\eta = 0$, 0.5, 1) and lidar ratios (S=20, 40, 60) in the aerosol correction.

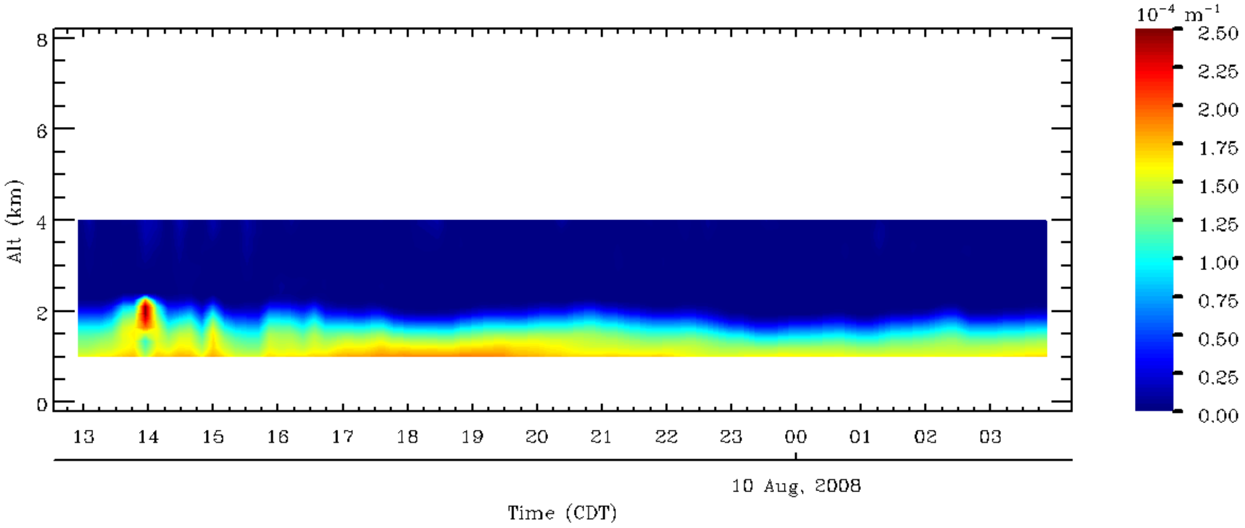

Alt (km)
0
2
4
6
8
13
14
15
16
17
18
19
20
21
22
23
00
01
02
03
10 Aug, 2008
Time (CDT)
10^{-4} m^{-1}
2.50
2.25
2.00
1.75
1.50
1.25
1.00
0.75
0.50
0.25
0.00

(a)

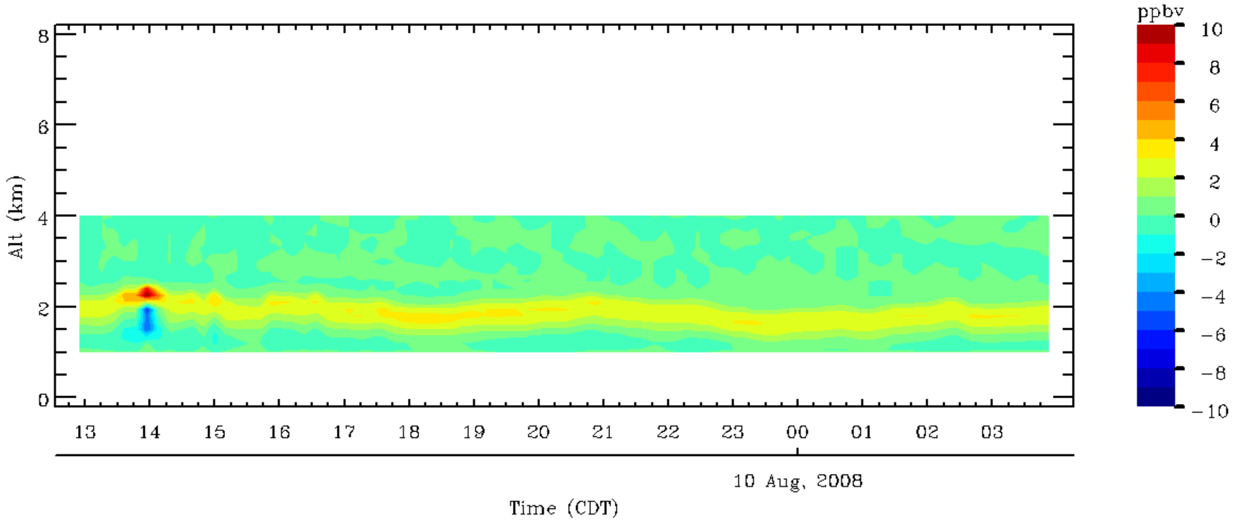

Alt (km)
0
2
4
6
8
13
14
15
16
17
18
19
20
21
22
23
00
01
02
03
10 Aug, 2008
Time (CDT)
ppbv
10
8
6
4
2
0
−2
−4
−6
−8
−10

(b)

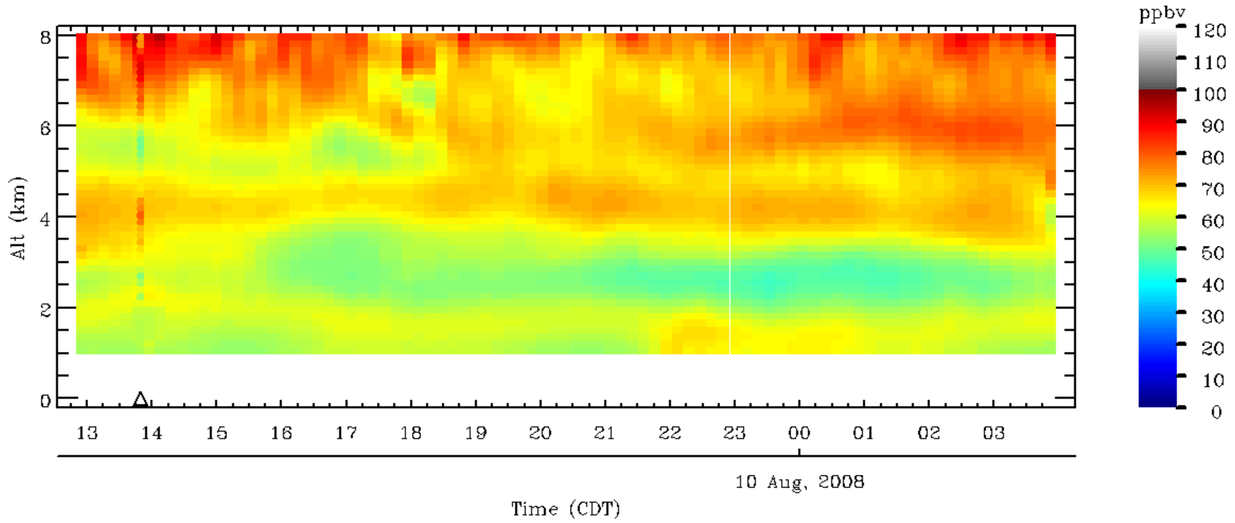

(c)

Figure 8. Ozone DIAL retrievals made on 9-10, Aug. 2008. (a) Calculated aerosol extinction coefficient at 291 nm. The feature at 2 km; 1400 is a cloud. (b) Aerosol correction for ozone DIAL retrieval. (c) Ozone DIAL retrieval after aerosol correction. The retrieval was made with a 750-m vertical range resolution and a 10-min temporal resolution. The co-located ozonesonde marked by a triangle launched at 13:49 local time.

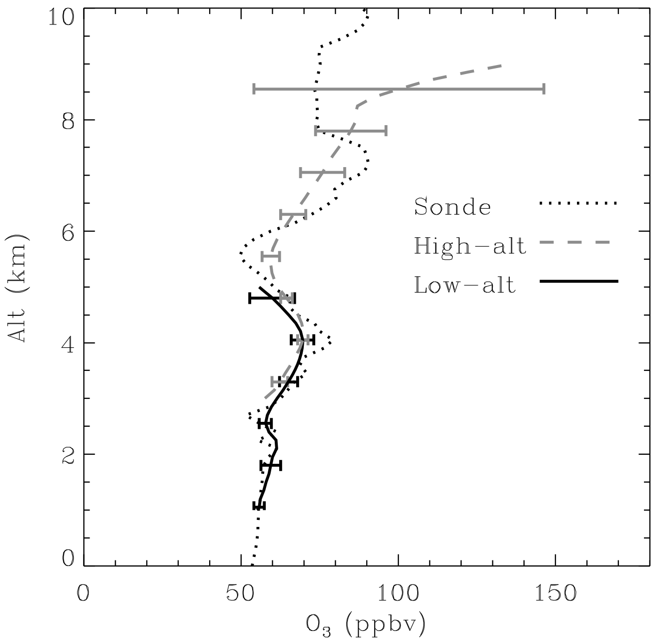

Figure 9. Mean ozone mixing ratio and 1-sigma standard deviation for the 10-min vertical profiles between 12:56 and 15:06 local time (excluding one cloudy profile at ~1400) in Figure 8. The co-located ozonesonde launched at 13:49 local time. Large error bar (~45%) at 8.5 km identifies the high-altitude limit of retrievals (8 km).

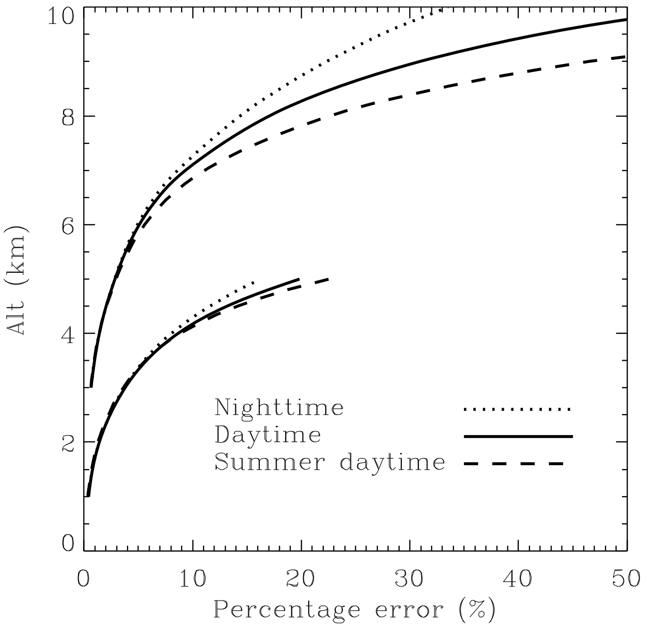

Figure 10. Estimated statistical errors for the high-altitude and low-altitude channels using 10-min integration and 750-m range resolution. The nighttime and daytime statistical errors are modeled by using the annually averaged local ozonesonde profile, the 1976 U.S. Standard Atmosphere, an urban aerosol model [78] and the lidar parameters in table 1. The ozone profile used for summer daytime errors is assumed 20% higher than the annual average.

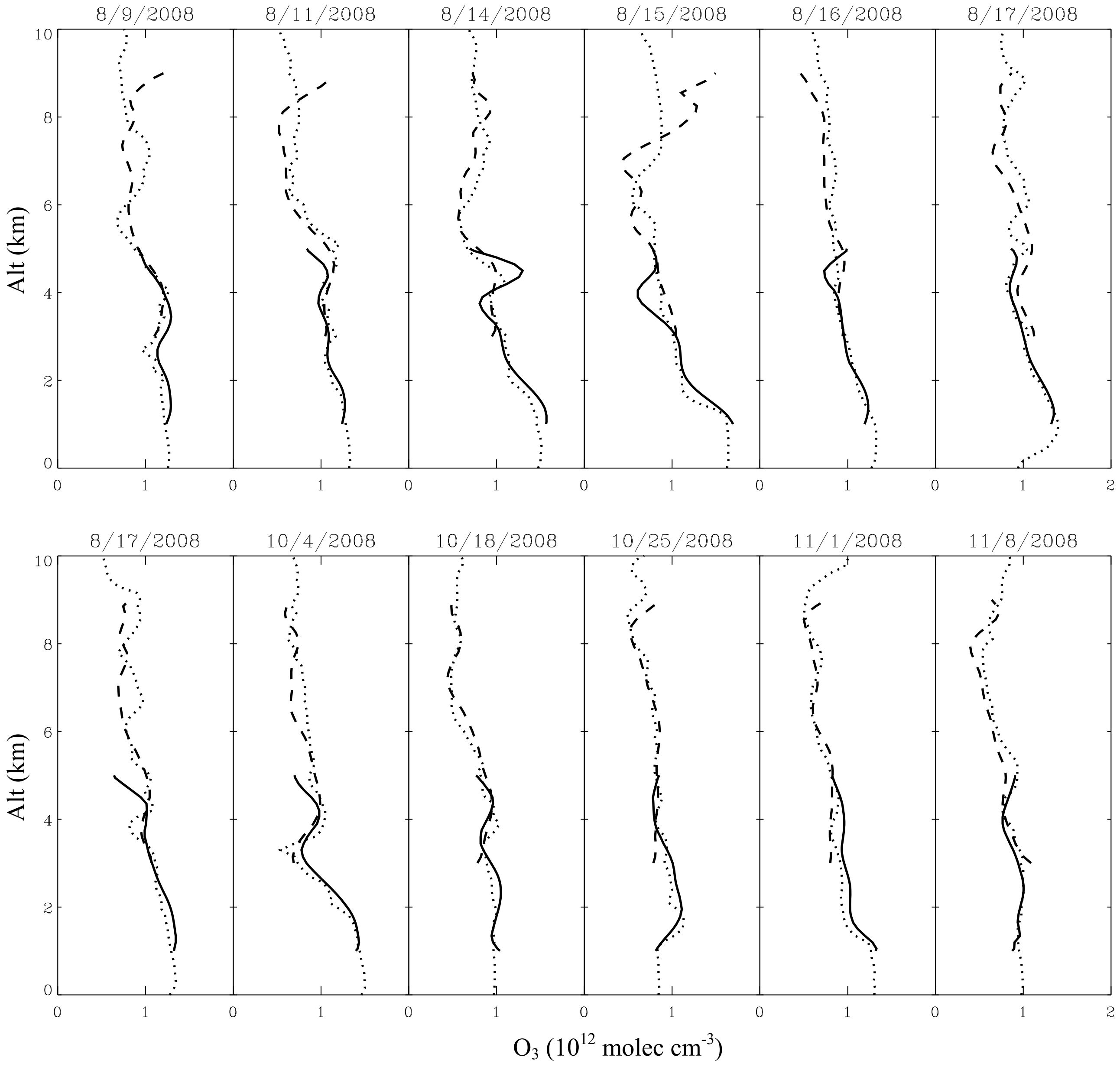

Figure 11. Comparison of the low-altitude (solid) and high-altitude (dash) channel aerosol-corrected retrievals with the coincident ozonesonde (dot) measurements.

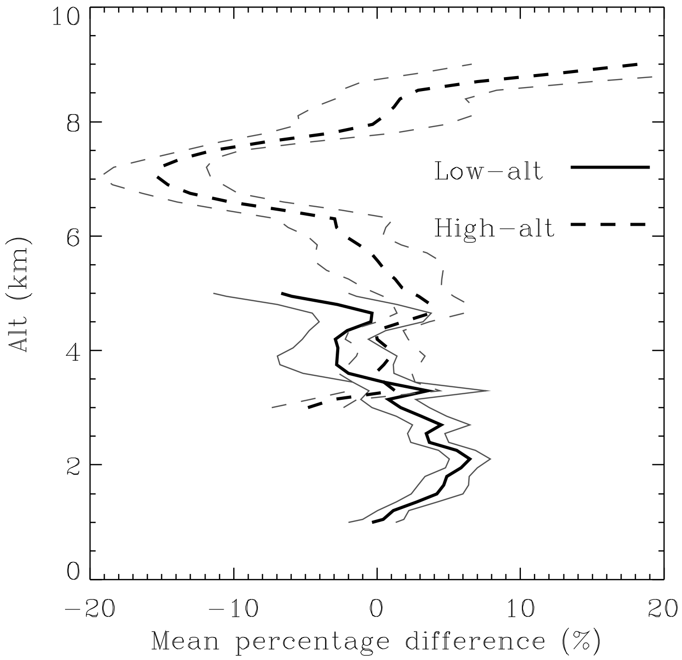

Figure 12. Mean percentage differences (dark) and their estimated 1-sigma standard error of the mean (gray) for the data in Figure 11.

Table 1. Characteristics of the RAPCD ozone DIAL system

System	Specification	
Transmitter		
Pump lasers	Nd:YAG, 20 Hz repetition rate, 5-7 ns pulse length, 300 mJ pulse^{-1} at 1064 nm, 50 mJ pulse^{-1} at 532 nm	
Dye	Rhodamine 590 and 610	
Emitted UV	4 mJ pulse^{-1} at 285 nm, divergence<1 mrad 3 mJ pulse^{-1} at 291 nm, divergence<1 mrad	
Tuning range	277 to 303 nm for the final UV output	
Receiver	High-altitude channel	Low-altitude channel
Telescope	Newtonian, 40-cm diameter, f/4.5, 1.5-mrad FOV	Welch Mechanical Designs Cassegrain, 10-cm diameter, f/2.3, 4.3-mrad FOV
Band-pass filter	Center wavelength at 286.4 nm with a 11-nm FWHM. Transmittance is 35% at 285 nm and 20% at 291 nm	
Detector	Electron Tubes 9813QA, about 28% quantum efficiency	Hamamatsu R7400U-03, about 20% quantum efficiency
Signal processing	LICEL Transient Recorder (TR40-80), 250-MHz maximum photoncounting rate, 12-bit and 40-MHz analog-to-digital converter, 25-ns range resolution	

Table 2. DIAL retrieval errors due to non-ozone absorption gases

Gases	$\Delta\sigma$, differential absorption cross-section (cm^2 $molec^{-1}$) for 285 and 291 nm	References for $\Delta\sigma$	Mixing ratio (ppbv)	References for mixing ratio	O_3 retrieval error (%)
O_3	1.15×10^{-18}	Bass and Paur 1981 [76]	60		
O_2[a]	4.5×10^{-27}	Fally et al. 2000 [79]	2.1×10^{8}		1.5%
SO_2	-4.8×10^{-20}	Rufus et al. 2003 [80]	13[b]	NREM 2006 [81]	-0.9%
NO_2	-2.25×10^{-20}	Bogumil et al. 2003 [82]	18[c]	NREM 2006 [81]	-0.6%
Total					±1.5%

[a] due to O_2-O_2

[b] maximum 24-hr average in 1994. Latest local monitoring data available.

[c] Annual arithmetic average in 1993. Latest local monitoring data available.

Table 3. Summary of the errors in RAPCD ozone DIAL measurements*

Errors	Low-altitude channel (1-4 km)	High-altitude channel (3-8 km)
1. ε_1, statistical error	<10%	<25%
2. ε_2, interference by non-ozone species		
Aerosol	<20%	<5 %
Non-ozone absorption gases	<1.5%	
Rayleigh	<1% using local radiosonde profile	
3. ε_3, due to uncertainty in $\Delta\sigma_{O3}$	<3%	
4. ε_4, due to SIB and dead-time	<5%	<10%
Total RMS error	<23%	<28%

* The errors are estimated by assuming a 60 ppbv constant ozone mixing ratio in the troposphere for data with a 750-m vertical resolution and 10-min integration.